Influence of crystallographic structure and metal vacancies on the oxygen evolution reaction performance of Ni-based layered hydroxides

Roger Sanchis-Gual,[1a] Diego Hunt,[2a] Camilo Jaramillo,[1] Alvaro Seijas-Da Silva,[1] Martín Mizrahi,[3,4] Carlo Marini,[5] Víctor Oestreicher,[1,*] Gonzalo Abellán[1,*]

[1] Instituto de Ciencia Molecular (ICMol), Universidad de Valencia, Catedrático José Beltrán 2, 46980, Paterna, Valencia, Spain.

[2] Departamento de Física de la Materia Condensada, GIyA. Instituto de Nanociencia y Nanotecnología, CNEA-CAC-CONICET. Av. Gral. Paz, 1650, San Martín, Buenos Aires, Argentina.

[3] Instituto de Investigaciones Fisicoquímicas Técnicas y Aplicadas (INIFTA), Departamento de Química, Facultad de Ciencias Exactas. Universidad Nacional de La Plata, CCT La Plata- CONICET. Diagonal 113 y 64, 1900, La Plata, Argentina.

[4] Facultad de Ingeniería, Universidad Nacional de La Plata. Calle 1 esq. 47, 1900, La Plata, Argentina.

[5] CELLS−ALBA Synchrotron, Cerdanyola del Vallès, 08290, Barcelona, Spain.

[a] Both authors contributed equally to this work.

Corresponding authors email: victor.oestreicher@uv.es, gonzalo.abellan@uv.es

Nickel-based layered hydroxides (LHs) are a family of efficient electrocatalysts for the alkaline oxygen evolution reaction (OER). Nevertheless, fundamental aspects such as the influence of the crystalline structure and the role of lattice distortion of the catalytic sites remain poorly understood and typically muddled. Herein, we carried out a comprehensive investigation on α-LH, β-LH and LDH phases, analysing the role exerted by Ni-vacancies by means of structural, spectroscopical, *in-silico* and electrochemical studies. Indeed, density functional theory (DFT) calculations, in agreement with X-ray absorption spectroscopy (XAS), confirm that the presence of Ni-vacancies produces acute distortions of the electroactive Ni sites (shortening in the Ni-O distances and changes in the O-Ni-O angles), triggering the appearance of Ni localised electronic states on the Fermi level, reducing of E_{gap}, and therefore increasing the reactivity of the electroactive sites. Furthermore, *post-mortem* Raman and XAS measurements unveil the transformation of α-LH phase into a highly reactive oxyhydroxide-like structure stable under ambient conditions. Hence, this work pinpoints the critical role of cationic vacancies on the structural and electronic properties of the LH structures, which controls their inherent reactivity towards OER catalysis. We envision Ni-based α-LH as a perfect platform for trivalent cations hosting, closing the gap toward the next generation of benchmark efficient earth-abundant electrocatalysts.

Introduction

Water electrolysis is considered one of the cleanest ways for producing hydrogen.[1–3] Nevertheless, its production also involves the oxygen evolution reaction (OER), an electrochemical process that requires high voltages because of slow kinetics. This process represents an important energetic efficiency loss in water-splitting systems and necessitates the use of inexpensive catalysts to reduce the energy barriers.[4,5] In this regard, the last decade has witnessed efforts in the development of earth-abundant electrocatalysts to reduce energy costs, with nickel-based materials emerging as one of the most widely used among the reported non-precious metal OER catalysts.[6]

Layered hydroxides (LHs) have been demonstrated to be outstanding OER electrocatalysts.[7–10] In addition to their exciting electrochemical features, they are easily scalable up, affordable and composed of non-geolocalised abundant elements.[11–14] Furthermore, their high chemical versatility has allowed for the fabrication of compounds with improved parameters, thereby boosting the OER. Along this front, the effect of different morphologies,[15] interlayer spaces,[16] metallic compositions,[17] clustering and structural instabilities,[18] to name a few, have already been investigated. Catalytic improvements are typically the result of increased surface areas, the ability to adsorb OH ions, diffusion properties, and/or the intrinsic activities of electroactive sites. Nowadays, many parameters influencing the OER are still not completely well understood or even explored. In particular, fundamental aspects such as the specific role of the crystalline LH structure, as well as the coordination environment and cation distortions, have not been comprehensively studied.

This is quite striking given the variety of crystalline structures that LHs can exhibit, especially since these aspects have been thoroughly investigated for Ni-based spinels and perovskites, demonstrating that both Ni atom configuration, as well as the crystal structure, have a significant impact on the OER electrocatalysis.[19,20] For example, in the case of strain-stabilised nickel hydroxide nanoribbons the modification of Ni coordination has a remarkable reduction in the overpotential for both OER as well as methanol oxidation reaction (MOR).[19,20] Therefore, the role of the structure and chemical environments in Ni-based LHs emerge as critical to enhance the OER electrochemical activity and stability of these earth-abundant compounds.

In this contribution, we have synthesised and fully characterised Ni-based LHs in the form of the non-expanded β-LH (*brucite*-like structure), and the expanded α-LH and LDH (*hydrotalcite*-like structure) to assess the role of the crystallographic structure on the OER performance. This is particularly relevant because α-LH phases are often confused with LDH.[21–24] According to structural and theoretical characterisation, Ni vacancies in the α-LH phase affect the structural and electronic properties of the LH structure, making it more conductive. In this regard, the electrochemical characterisation confirms a superior catalytic behaviour of α-LH in comparison to the other phases. Specifically, the onset potential (OP<50 mV for α-LH) is considerably reduced and the kinetics of the reaction are greatly enhanced due to the inherent high reactivity imposed by the presence of Ni vacancies, which makes the electroactive sites more reactive, as confirmed by XAS. These findings demonstrate that the crystallographic features play a key role in the electrochemical behaviour of LH phases, pinpointing a new chemical signature for the rational design of more efficient electrocatalysts.

Results and Discussion

As we have recently reported for Co-based LHs, the role of crystallographic structure can play a crucial role in the OER performance, even in those phases containing exclusively Co^{II} cations.[25] Thus, considering our last finding and the importance of nickel in the development of OER catalysts, we decided to perform a comprehensive study on the most important Ni-based LHs: *brucite*-like (β-LH), *hydrotalcite*-like (LDH), and turbostratic-like (α-LH). In the case of the non-expanded β-LH phase, cations adopt octahedral environments, $M^{II}(O_h)$, exclusively, and exhibit basal space distances (d_{BS}) lower than 5 Å.[26–28] Without any doubt, the most famous member of the LH family are layered double hydroxides (LDHs), also known as cationic clays.[12,29] This phase is composed of positively-charged layers containing divalent and trivalent cations located in octahedral environments, $M^{II}(O_h)$ and $M^{III}(O_h)$, respectively. Due to the charge excess, anions and solvent molecules are incorporated in the interbasal space, expanding the d_{BS} to values greater than 7 Å, obeying the chemical formula $M^{II}_{1-x}M^{III}_{x}(OH)_2 A^{n-}_{x/n}\cdot m(H_2O)$. Considering the purely electrostatic anion-sheet interaction, plenty of different LDHs can be obtained by exchange reactions, resulting in countless interesting materials for several applications, being nowadays energy storage and conversion the most studied ones.[7,14,29] Additionally, α-LH phases, also known as basic salts, are expanded structures containing anions in the interlayer space.[30,31] The specific crystallographic structure of α-LH phases, as well as the anion-sheet interaction, strongly depends on the nature of the divalent cations, adopting either octahedral (O_h) or tetrahedral (T_d) environments as in the case of Co-based LHs. However, the Ni-based α-LH consists of a turbostratic layered hexagonal structure containing $Ni^{II}(O_h)$, exclusively, as displayed by the formula $Ni^{Oh}(OH)_{2-x} A^{n-}_{x/n}\cdot m(H_2O)$.[28] Additionally, this layered compound also owns anion exchange properties as in the case of LDHs, even despite the absence of trivalent cations.[32] Figure 1 exemplifies through a schematic representation each Ni-based LHs structure, highlighting their main features. Importantly, since the idea of this work lies in understanding the relationship between the crystallographic structures and electrocatalytic performance, LH phases containing exclusively Ni^{II} as divalent cations are considered. In this regard, an LDH phase containing non-electrocatalytic trivalent cations such as $Al^{III}(O_h)$ is used as a model system.

Ni-based LH phases were obtained through well-established synthetic protocols (see "LH synthesis", in SI). Figure 2 compiles the complete chemical and structural characterization of all samples by Powder X-Ray Diffraction (PXRD), Attenuated total reflectance Fourier-transform infrared spectroscopy (ATR-FTIR), X-Ray photoelectron spectroscopy (XPS), UV-Vis spectroscopy and synchrotron X-Ray absorption spectroscopy (XAS).

The PXRD patterns depicted in Figure 2A confirm the layered nature of LHs phases as it can be observed by the presence of the reflections at lower 2-*theta* values, indexed as $00l$. The obtained d_{BS} values are around 4.65, 7.36 and 10.15 Å for β-LH, LDH and α-LH phases, respectively. Furthermore, the reflections labelled as 110 are assigned to the intralayer parameter ($a = 2 \cdot d_{110}$), providing information related to the *in-plane* cationic distances, exhibit values centred at 1.565, 1.510 and 1.545 Å for β-LH, LDH and α-LH phases, respectively. In the case of the LDH phase, this value is lower than β-LH and α-LH, as expected by the incorporation of a smaller cation as Al^{III} into the layers ($Ni^{II}_{Oh} = 0.690$ Å; $Al^{III}_{Oh} = 0.535$ Å).[33] Table S1 compiles the cell parameters as a function of LH phases which are in agreement with previous reports.[23,26,27,34,35]

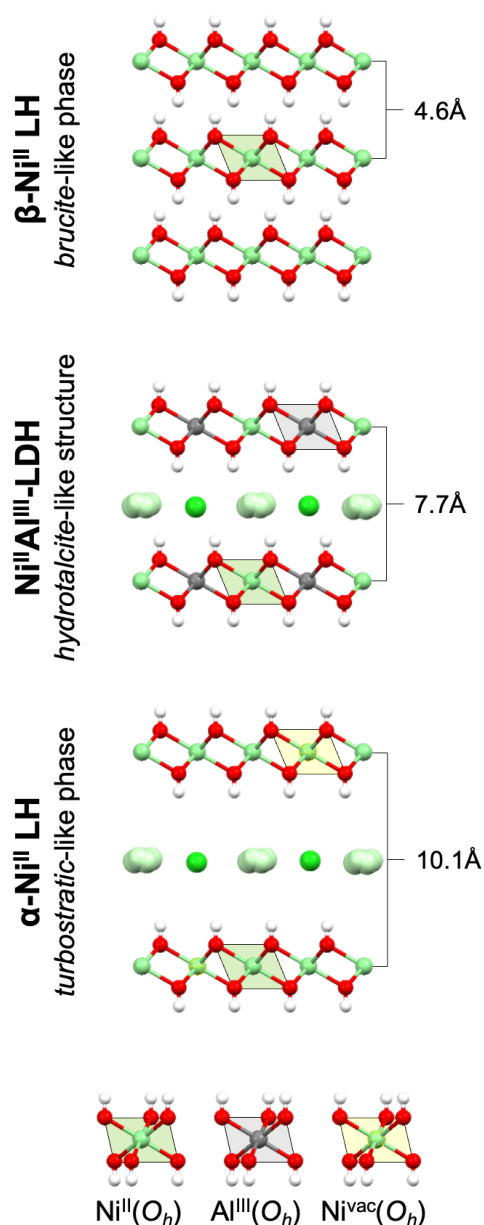**Ni^{II}-based layered hydroxides**

Figure 1. Schematic representation of the different crystallographic structures for Ni-based layered hydroxides studied in this work, highlighting their main differences and reported basal space distances (d_{BS}). Note: $Ni^{vac}(O_h)$ represents a cationic vacancy.

ATR–FTIR also provides structural information of each LH phase, as shown in Figure 2B. The β-LH phase can be distinguished by the presence of an intense and sharp band at around 3630 cm^{-1} attributed to the O-H stretching mode, characteristic of free-OH groups in *brucite*-like structures.[36] In the case of the expanded structures, the presence of interlayer water molecules can be confirmed by the broad band centred at *ca*. 3400 cm^{-1} (O-H stretching mode) and an extra peak at around 1600 cm^{-1} (H_2O bending mode). The sharper band observed in the α-LH phase is attributed to a higher water confinement degree.[24] In the particular case of LDH structure, the bands at 1345 and 800 cm^{-1} confirm the incorporation of carbonate molecules as expected considering the synthetic method, which employed urea as an alkalinisation agent.[37] Finally, signals below 1000 cm^{-1} are associated

with M-O stretching and M-OH bending vibrations. Interestingly, whatever the cation, these vibrations strongly depend on the LH phase's identity, resulting in an easy fingerprint to identify them. Table S2 compiles the most characteristic vibrations band for all the LH samples.

XPS was employed to gain further information about the chemical speciation and composition of the samples (Figure 2C). As expected, the occurrence of Ni^{II} is supported by its main peaks at 856±0.1 eV ($2p^{3/2}$) and 873.5±0.1 eV ($2p^{1/2}$).[38] However, besides the oxidation state, no appreciable differences are noticeable, suggesting that XPS is not the most appropriate technique for identifying the nature of Ni-based LHs.[39]

On the other hand, UV–vis diffuse reflectance spectroscopy is a suitable technique in LH characterisation since it can provide information about both metallic coordination environments and oxidation states (Figure 2D), as we have demonstrated for Co-LHs structures.[21,40–42] In this regard, Ni-based LHs depict two sets of wide bands positioned around 400 and 700 nm for $Ni^{II}(O_h)$, which are assigned to $^3A_{2g}$ to $^3T_{1g}(P)$, $^3T_{1g}(F)$, and $^1E_g(D)$ transitions.[23] Interestingly, the bands ascribable to O_h environments evidence slight differences for each LH phase, which alert about changes in the electronic structure, while at the same time can provide an easy LHs fingerprint for its identification. Figure S1 and Table S3 compile the bands' position for each LH sample.

To further characterise this Ni-based LH family, XAS measurements were conducted in CLÆSS BL22 beamline at ALBA Synchrotron. Figure 2E displays the X-ray Absorption Near Edge Structure (XANES) spectra for the Ni-K edge. All the samples contain exclusively Ni^{II}, as expected the position of the absorption edges (in grey). The Extended X-ray Absorption Fine Structure (EXAFS) regions have been analysed to extract further structural details. Figure 2F depicts the Fourier Transform (FT) of the EXAFS oscillations at the Ni K-edge. For all the samples, the two major contributions, located in the 1–3 Å range, represent the average distances (without phase correction) to the first and second coordination shells around the nickel atoms. At first glance for all the samples, Ni^{II} moieties are located in O_h environments, as expected; exhibiting Ni-O distances of 2.09 Å for β-LH and LDH, and 2.06 Å for α-LH.[31] Additionally, the marked reduction in the second peak amplitude for the LDH sample is related to the presence of Al cations, due to destructive interferences. Structural parameters such as coordination numbers (N), interatomic distances (R), and structural disorder (σ^2), were obtained through EXAFS fittings by assuming: (*i*) a single Ni-O distance for O_h cations; (*ii*) a shell of Ni and/or Al as second neighbours according to each sample. The obtained parameters can be found in Table S4, SI. The average coordination number for β-LH and LDH is *ca.* 6 for the second shell, as expected considering the crystal structures. However, the α-LHs sample exhibits a much lower value of 5.1. Since Ni^{II} cations are exclusively in octahedral sites, the existence of Ni vacancies could lead to a decrease in the Ni-Ni coordination number. This assumption is also in agreement with the higher structural disorder found for this shell/sphere (σ^2_{Ni-Ni} = 0.011 Å^2) which can be associated with a rearrangement of Ni atoms near the vacancies (see Table S4, SI).

Hence, the establishment of Ni-based LHs exhibiting non-expanded and expanded structures (*i.e.* β-LH *vs.* LDH & α-LH, respectively), containing exclusively Ni^{II} in octahedral environments can be concluded, where the α-LH phase exhibits cationic vacancies.[43]
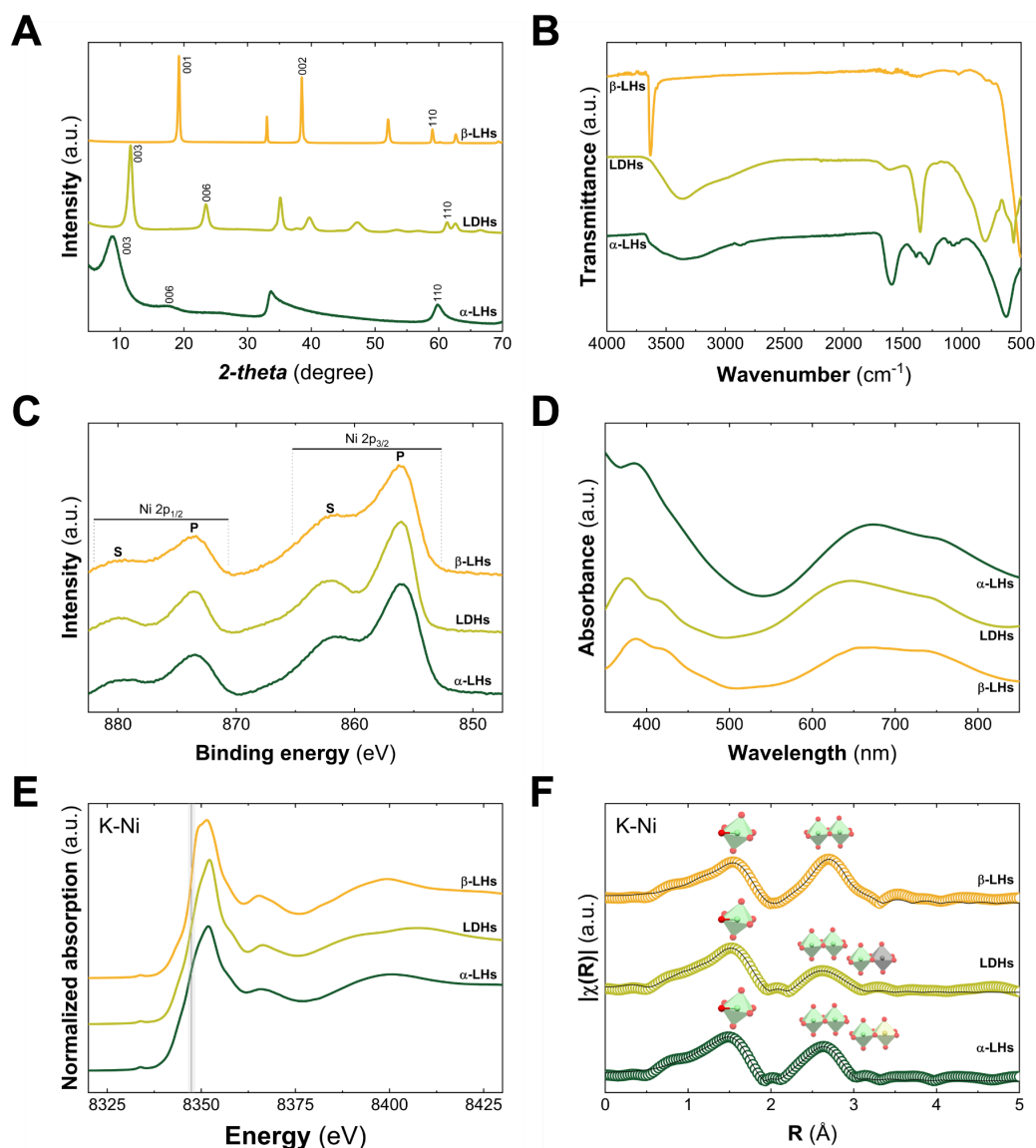
Figure 2. Structural characterisation of Ni-based LHs. (A) PXRD patterns underline the layered nature of the structures, as denoted by the *00l* reflections, while intralayer distance (*a*) is denoted by the 110 reflections. (B) ATR-FTIR spectra depict a clear change in the water-related band, highlighting the presence of intralayer water. (C) High-resolution XPS for Ni 2p ($2p^{3/2}$ and $2p^{1/2}$) in the range 880 – 850 eV. (D) UV-Vis spectra point out the marked differences in the nickel octahedral environments, $Ni^{II}(O_h)$. Normalised XANES spectra at the Ni K-edge. The black line depicts the expected position for nickel atoms exhibiting oxidation state +2 (E). κ^2-weighted Fourier transform of the extracted EXAFS oscillations, for the measured samples -circles- and their corresponding fittings -black line-. The first peaks are attributed at Ni-O distances (green octahedrons). Second peaks consider the Ni-Ni distances (green-green polyhedrons) in the case of β-LHs and α-LHs, and Ni-Ni (green-green polyhedrons) and Ni-Al (green-grey polyhedrons) ones for LDH (F). The reduction in the intensity for the second peak in the case of α-LHs is attributed to the presence of Ni vacancies (light green polyhedrons). All the XAS spectra are represented without phase correction.

To delve into the structural parameters and electronic properties of Ni-based LH phases from a microscopic point of view, *ab-initio* calculations based on density functional theory with Hubbard's correction (DFT+U) have been performed. Remarkably, the mineral nickel hydroxide is found in nature in the form of *brucite*-like structure known as *theophrastite*.[44–46]

Firstly, we decided to compare our DFT+U simulation for a $\beta - Ni_{DFT+U}$ cell with the

structural parameters present in *theophrastite* phase. After performing atomic relaxations on $\beta - Ni_{DFT+U}$ cell, our results show that the optimised Ni-O and Ni-Ni distances, as well as the most relevant O-Ni-O angles, exhibit an excellent agreement with the *theophrastite* phase (see Figure S2 and Table S5). For α-LH phase, there are no reported mineral structures, and additionally, fundamental structural and electronic aspects for this phase are still a matter of discussion.[28] Hence, considering the presence of Ni vacancies in this structure, as confirmed by EXAFS measurements (Figure 2F),[31,43] we decided to evaluate the role of vacancies in the structural and electronic properties through DFT+U calculations. It is important to remark that our proposition, the $\beta - Ni_{DFT+U}^{vacancy}$ cell, is a simplified simulated structure, being assumed as a first approximation to the real structure of α-LH phase.

At a first glance, the introduction of Ni vacancies at $\beta - Ni_{DFT+U}$ cell has a great impact on the structural nature of the sheet, producing strong distortions which affect the octahedral environment of Ni^{II} as can be noticed by the changes in interatomic distances and angles (Figure 3A). In the case of the distances, the optimised $\beta - Ni_{DFT+U}^{vacancy}$ cell presents a marked shortening in both Ni-O and Ni-Ni distances in comparison to $\beta - Ni_{DFT+U}$ and, therefore the *theophrastite* phase. Interestingly, these theoretical values are in perfect agreement with the contraction of the *a* parameter observed by PXRD measurements (Figure 2A and Table SX), as well as the shortening in Ni-O and Ni-Ni distances obtained by EXAFS analysis (Figure 2F and Table S4), suggesting that $\beta - Ni_{DFT+U}^{vacancy}$ cell can be considered as a good first approximation to study the structural properties of Ni-based α-LH phase. Furthermore, the structural distortions concomitantly modify the O-Ni-O and Ni-O-Ni angles (Figure 3A). Indeed, the optimised structure for the $\beta - Ni_{DFT+U}^{vacancy}$ cell reveals the presence of two kinds of octahedral Ni^{II} cations: a first set of Ni^{II} moieties neighbouring to the vacancy (labelled as Ni_{α}) and the second set of Ni^{II} sites next-nearest-neighbour to vacancy (Ni_{β}). While Ni_{α} environments, only present in the $\beta - Ni_{DFT+U}^{vacancy}$ cell, are strongly modified by the presence of the vacancy; Ni_{β} environments are equivalent to those ones found in the *theophrastite* phase and both $\beta - Ni_{DFT+U}$ and $\beta - Ni_{DFT+U}^{vacancy}$ cells. Hence, these differences in the geometrical sites for Ni^{II} cations may explain the observed changes in the optical properties, exemplified by UV-Vis spectroscopy (Figure 2D).

After assessing the structural aspects, we studied the electronic properties. In this sense, a band gap of approximately 2.2 eV is observed in the case of the $\beta - Ni_{DFT+U}$ cell, evidencing an insulator behaviour from the electronic point of view (Figure 3B). An inspection around the Fermi level suggests that the valence band is mainly dominated by *p* orbitals of oxygen atoms, while conduction bands have a large contribution from the *d* orbitals of Ni cations. As previously mentioned, Ni vacancy generation has a great impact on the structure which modifies the Ni-O and Ni-Ni distances, as well as the O-Ni-O and Ni-O-Ni angles, resulting in changes in the electronic properties. Indeed, these lattice distortions produce an insulator-metal transition in which both the *p* orbitals of oxygen atoms and the *d* orbitals of Ni atoms shift to the Fermi level. Interestingly, recently we have reported for α-NiCo LHs that the distortion of octahedral environment triggered by Co-O distances shortening, can promote the population of the Fermi level with *d* states from distorted Co, enhancing their reactivity towards oxidation; reinforcing the idea that the so-called *"cis distortion"* can modify the electronic nature of layered materials.[23] Additionally, similar electronic behaviour has been observed for NiFe LDHs nanosheets by the introduction of Ni vacancies.[47] Although,

these results strongly suggest that the presence of Ni vacancies of hydroxylated Ni-based layers would deeply modify the structure, electronic behaviour, and therefore the electrocatalytic performance; strictly speaking, it is important to note that the $\beta - Ni_{DFT+U}^{vacancy}$ cell is a simplified structure for the α-LH phase, and therefore further work is required to provide a comprehensive description of α-Ni LH.
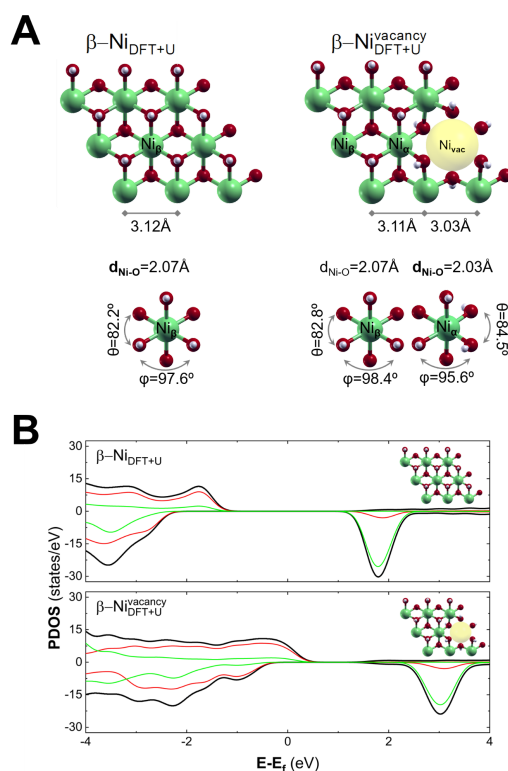

Figure 3. DFT+U simulations for a single layer of *brucitic*-like Ni(OH)$_2$ structure ($\beta - Ni_{DFT+U}$) and the resulting one after the Ni vacancies generation ($\beta - Ni_{DFT+U}^{vancancy}$). (A) Relaxed structures for both supercell highlight that while β-Ni contains only one cationic environment (Ni$_\beta$), in the case of β-Ni^{vacancy} presence of two different Ni sites are observed: Ni$_\alpha$, for the atom around the vacancy, and Ni$_\beta$ for the other ones. Calculated structural parameters, such as Ni-O and Ni-Ni distances and angles for both supercells are shown. (B) Total and Projected Density of States (PDOS) for a layer of β-Ni(OH)$_2$ structure (upper panel) and the resulting one after the generation of Ni vacancies (lower panel). Atoms are labelled according to Figure 1: H -white-, O -red-, Ni -green-, Ni vacancy -yellow-.

After the structural and electronic description, we performed the electrochemical characterisation of all the samples under alkaline oxygen evolution reaction (OER) conditions, by employing a three-electrode cell (glassy carbon electrode to avoid catalyst-electrode transformation)[48] using 1 M KOH aqueous solution (Figure 4). Firstly, we proceeded by activating the electroactive material through 30 steps of cyclic voltammetry at 50 mV/s. Remarkably, the cyclic voltammetry curves have a specific shape for each LH sample, suggesting a distinct redox nature for each Ni site, the electroactive species (Figure 4A-C). In addition, the activation process can be followed by analysing the cathodic charge in each cyclic voltammetry curve (Figure 4D). The α-LH sample exhibits the largest activation process (3000% increment with respect to the first cycle), in comparison to LDH (100%) and β-LH (35%). Thus, the superior α-LH activation highlights its inherent chemical

nature towards oxidation, which can be mainly related to the presence of Ni vacancies (and the electronic properties).
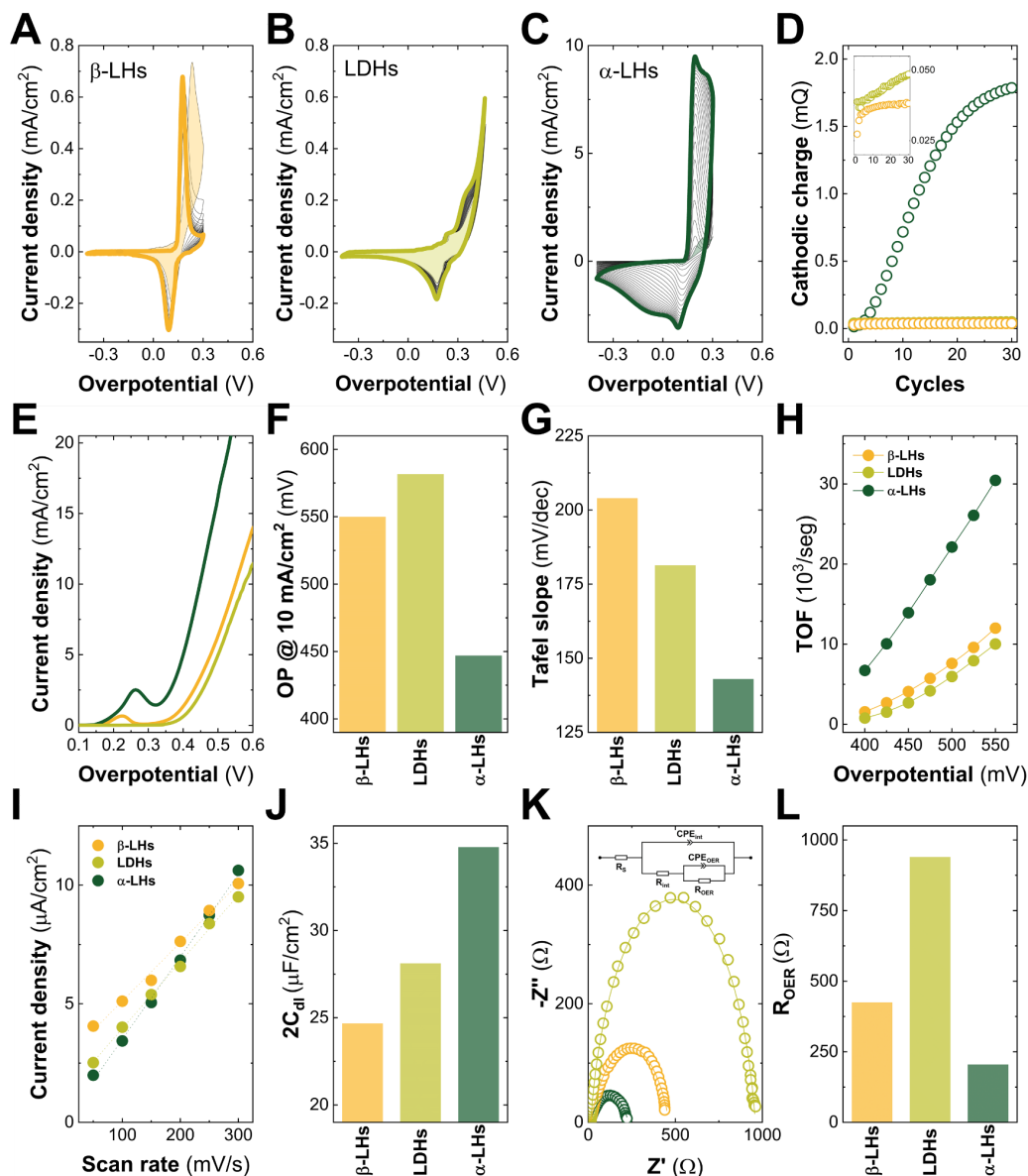

Figure 4. Activation processes were carried out before the OER experiments and consisted of 30 cyclic voltammetry curves performed in a KOH 1 M aqueous solution at 50 mV/s for each Ni-based LH structure (A, B and C). Note the order of magnitude of the *y-axis*. The first cycles are depicted as shading curves, while the final ones are presented by thick coloured lines. The shape of the curves as well as their evolution are the first indication of the relationship between structure and electrochemical performance. Evolution of the cathodic charge of the different Ni-based LH structures during the activation processes carried out before the OER experiments (D). Electrochemical characterisation for Ni-based LH family recorded on a glassy carbon electrode collector. Linear sweep voltammetry curves measured at 5 mV/s in 1 M KOH aqueous solution (E). Overpotential values required for a current density of 10 mA/cm^2 (F). Tafel slopes values calculated from LSV data (G). Turnover frequency values obtained as a function of overpotential (H). Linear slopes representing the ECSA calculated from CVs performed in a non-faradaic region at different scan rates (I). ECSA values of the different structures (J). Nyquist plots of the different samples recorded at an overpotential of 0.4 V. Points correspond to experimental data, and lines are curves fitted with the equivalent circuit. Inset: equivalent circuit used (K). Resistance values of the process associated with the OER. The resistance values were estimated from the equivalent circuit (L).

Once the samples were activated, the electrochemical water splitting performance was characterised by measuring linear sweep voltammetry (LSV) at a slow scan rate. The non-*iR* corrected (*iR*, with R = 2 ± 1 Ω) overpotential curves measured up to 0.6 V are represented in Figure 4E. Three key parameters were extracted from the LSV curves at least by triplicate to analyse the OER performance: (*i*) the overpotential (OP) required to get 10 mA/cm^2 (Figure 4F), (*ii*) the Tafel slopes (Figure 4G); and (*iii*) the turnover frequency (TOF) values (Figure 4H), calculated at the overpotential range of 400–525 mV. By comparing all these aforementioned parameters, we can conclude that α-LH arises as the better electroactive material, exhibiting OP values *ca.* 100 mV lower, smaller Tafel slope (*ca.* 32%), and TOF values almost three-fold higher (see Table S6). These results are in good agreement with the ones from the activation process, reinforcing the idea of a higher inherent chemical nature of the α-LH samples towards electrocatalysis.

Additionally, the electrochemical surface area (ECSA), corresponding to the double-layer capacitance, was extracted from fitted plots (Figures 4I and 4J). This value gives an estimation of the number of electroactive centres in the electrocatalyst. In this line, the α-LH phase exhibits an ECSA value around 30–40% larger than the other compounds and thus, it has a higher number of electroactive species able to participate in the OER process, resulting in an enhancement of the electrochemical performance. Kinetics aspects were addressed by measuring Electrochemical Impedance Spectroscopy (EIS) and fitting the obtained results to an equivalent circuit (Figure 4K). Due to the possibility of surface roughness, physical non-uniformity, and non-uniform distribution of the electroactive sites, constant phase elements (CPEs) were introduced in this model to provide a good match with the experimental data. The equivalent circuit is composed of a resistance related to the ionic transport through the solution and the current collectors (R_S) connected in series with a first parallel branch (R_{int} and CPE_{int}) associated with the electrocatalyst-glassy carbon interfacial contact. These elements (R_S, R_{int} and CPE_{int}) are observed in the high-frequency region whereas, in the low-frequency region, OER processes occurring on the LH surface are represented by a second parallel branch (R_{OER} and CPE_{OER}). As can be observed from Figure 4L, the best values (i.e. the lowest resistances) are once again recorded for the α-LH structure. Indeed, the reduction of R_{OER} is the result of a higher number of active centres and intrinsic conductivity of the electroactive phase, which promotes oxygen formation. Note that for NiAl-LDH, the R_{OER} value is especially high, exceeding that of the β-LH structure. The low formation of the conductive and electroactive NIOOH phase during the OER process may be responsible for this high resistance value in the LDH compound.[49,50] Overall, the increase in the number of electroactive sites in combination with the diminution of the OER resistance results in the improvement of the onset potential, the kinetics of the electrocatalytic reaction, as well as the stability (see Figure S4, SI).

Considering the differences observed in terms of OER performances, we explored the evolution of the LH phases after the electrocatalytic process. The *ex-situ* characterisation of each LH sample was performed by Raman spectroscopy and PXRD *in-house* immediately after the OER process (less than 1h), while XAS was carried out after 5 days at ALBA synchrotron. To that end, the solid samples were deposited by spray coating on carbon paper (C_{paper}) electrodes and electrochemically characterised, obtaining trends similar to those observed on glassy carbon electrodes (see Figure S5, SI).

Figure 5A compares the Raman spectra for LH samples on carbon paper before and after the electrocatalytic process in the 100–1000 cm^{-1} range. Specifically, the main peaks around 400–600 cm^{-1} are assigned in all phases to M-O vibrations. Note that the sensitivity of these two peaks to structural changes in LH phases has been previously employed in OER studies.[51,52] The β-LH spectra suggest surface oxidation due to the apparition of a broad

peak centred at 500 cm^{-1}.[53] LDH spectra do not reveal any observable transformation, as expected considering its poor electrochemical performance. Whilst, in the case of the α-LH sample, the presence of two sharp signals at 476 and 558 cm^{-1} (denoted with asterisks) after OER catalysis evidences the transformation towards the electrocatalytic active NiOOH phase, as previously reported by *in situ* experiments. Furthermore, Figure 5B depicts the PXRD patterns of LH samples where structural modifications are clearly observed. For β-LH, besides the presence of unreacted β-Ni(OH)$_2$ signals, the apparition of a new peak at lower *2-theta* values related to an interlayer distance of 7.7 A highlights the partial transformation towards pure Ni-based LDH phase. Note that to the best of our knowledge, this is the first structural evidence of a Ni^{II}Ni^{III} LDH structure, pointing out that it would be possible to obtain this phase through topochemical oxidation.[27,54–56] Nonetheless, no changes were observed for the LDH sample. Interestingly, in the case of α-LH, the fading of 003 reflection related to this phase suggests a massive transformation toward oxyhydroxide-like phases triggered during the OER process.
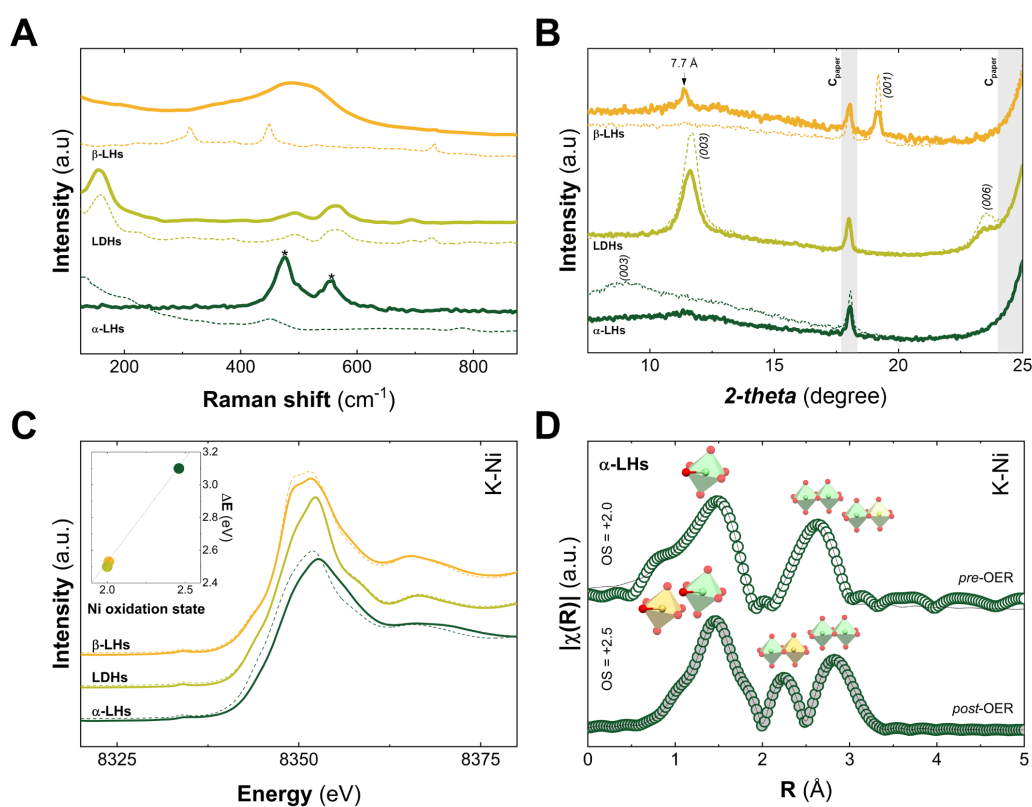

Figure 5. Post-mortem analysis: characterisation before (dashed line) and after (solid line) OER catalysis. (A) Raman spectra evidence the surface oxidation of the phases, meanwhile, in the case of α-LH structure, the twin peaks at 476 and 558 cm^{-1} (denoted with asterisks) confirm the transformation into NiOOH. (B) PXRD patterns denote non-changes in the bulk structure for β-LH and LDH phases, while in the case of α-LH sample, a massive transformation towards oxyhydroxide-like structure stable under ambient conditions is observable due to the $00l$ signal disappearance. Note: carbon paper substrate (C$_{paper}$) reflections are denoted in grey. Normalised XANES spectra at the Ni K-edge, before (dashed lines, pre-OER) and after (solid lines, post-OER) the OER measurements (C). Final oxidation states were calculated by Capehart's method after OER measurements and calibration curve (C-inset). (D) Pre- and post-OER κ^2-weighted Fourier transform of the extracted EXAFS oscillations for the measured samples –circles– and their corresponding fittings –black line– for α-LH sample. The first peaks are attributed at Ni-O distances: green for Ni^{II}(O$_h$) and orange for Ni^{III}(O$_h$). The second and third peaks consider the Ni-Ni distances, where polyhedrons represent: Ni^{II}(O$_h$) -in green-, Ni^{III}(O$_h$) -in orange-, and Ni vacancies (in light green). In all the cases the XAS spectra are represented without phase correction.

To further confirm the changes taking place in the LH samples during the OER catalysis, and aim to quantify them, *ex-situ* XANES spectra were compared before and after the electrocatalytic process (Figure 5C). Almost unnoticeable shifts in the position of the absorption edges are observed for β-LH and LDH samples. However, in the case of α-LH, the shifts become evident, pointing out that this phase is more prone towards oxidation as observed by Raman and PXRD. A precise quantification of the oxidation state was carried out by employing the integral method described by Capehart *et al* (Figure 5D).[57] Indeed, while β-LH and LDH do not surpass a final oxidation state higher than 2.1, α-LH sample exhibits a final average oxidation state of 2.5, remarkably stable under ambient conditions even after a week. Considering the calculated final oxidation states for β-LH and LDH, EXAFS analysis has been carried out on the α-LH sample, exclusively. At first glance, the first peak exhibits a shift towards lower distances, compatible with the Ni^{III} formation ($Ni_{Oh}^{II} = 0.69$ Å; $Ni_{Oh}^{III} = 0.60$ Å).[33] In the case of the second shell, the original peak splits in two new signals associated to two different Ni-Ni moieties. To quantify this information, a model considering two Ni-O and two Ni-Ni distances is proposed. The results of the fitting are presented in Table S7, SI. Thus, apart from the previously fitted distances for Ni-O and Ni-Ni of 2.1 and 3.1 Å, the new ones of 1.9 and 2.7 Å are in perfect agreement with the NiOOH formation, which represents approximately 50% of the sample, in concordance with the final oxidation state.[58–60]

Conclusion

Overall, our results confirm that the Ni-based α-LH structure is the most electroactive LHs catalyst containing exclusively Ni^{II} centres. The structural and theoretical characterisation suggests that the presence of Ni vacancies affects the structural and electronic properties of the LH phase making it a more reactive and conductive material, beyond nano-structuration.[19,20,61] Indeed, Ni vacancies are responsible for this electrochemical enhancement, triggering its transformation towards highly active and stable oxyhydroxide phases. We envision α-LH structure as the most appealing host for the incorporation of highly active trivalent cations such as Cr, V, Fe and Co in the search for highly electroactive Ni-based materials for water, methanol and/or ammonia oxidation, with great potential for industrial application.

Acknowledgements

References

[1] S. Chu, A. Majumdar, *Nature* **2012**, *488*, 294–303.

[2] Z. Yan, J. L. Hitt, J. A. Turner, T. E. Mallouk, *Proceedings of the National Academy of Sciences* **2020**, *117*, 12558–12563.

[3] M. F. Lagadec, A. Grimaud, *Nat. Mater.* **2020**, *19*, 1140–1150.

[4] F. Dionigi, Z. Zeng, I. Sinev, T. Merzdorf, S. Deshpande, M. B. Lopez, S. Kunze, I. Zegkinoglou, H. Sarodnik, D. Fan, A. Bergmann, J. Drnec, J. F. de Araujo, M. Gliech, D. Teschner, J. Zhu, W.-X. Li, J. Greeley, B. R. Cuenya, P. Strasser, *Nature Communications* **2020**, *11*, 2522.

[5] F. Dionigi, J. Zhu, Z. Zeng, T. Merzdorf, H. Sarodnik, M. Gliech, L. Pan, W.-X. Li, J. Greeley, P. Strasser, *Angewandte Chemie International Edition* **2021**, *60*, 14446–14457.

[6] V. Vij, S. Sultan, A. M. Harzandi, A. Meena, J. N. Tiwari, W.-G. Lee, T. Yoon, K. S. Kim, *ACS Catal.* **2017**, *7*, 7196–7225.

[7] D. Zhou, P. Li, X. Lin, A. McKinley, Y. Kuang, W. Liu, W.-F. Lin, X. Sun, X. Duan, *Chem. Soc. Rev.* **2021**, *50*, 8790–8817.

[8] Z. Cai, X. Bu, P. Wang, J. C. Ho, J. Yang, X. Wang, *J. Mater. Chem. A* **2019**, *7*, 5069–5089.

[9] L. Yang, Z. Liu, S. Zhu, L. Feng, W. Xing, *Materials Today Physics* **2021**, *16*, 100292.

[10] F. Dionigi, P. Strasser, *Advanced Energy Materials* **2016**, *6*, 1600621.

[11] F. Li, X. Duan, in *Layered Double Hydroxides* (Eds.: X. Duan, D.G. Evans), Springer, Berlin, Heidelberg, **2006**, pp. 193–223.

[12] S. He, Z. An, M. Wei, D. G. Evans, X. Duan, *Chem. Commun.* **2013**, *49*, 5912–5920.

[13] G. Fan, F. Li, D. G. Evans, X. Duan, *Chem. Soc. Rev.* **2014**, *43*, 7040–7066.

[14] J. Yu, Q. Wang, D. O'Hare, L. Sun, *Chem. Soc. Rev.* **2017**, *46*, 5950–5974.

[15] C. Luan, G. Liu, Y. Liu, L. Yu, Y. Wang, Y. Xiao, H. Qiao, X. Dai, X. Zhang, *ACS Nano* **2018**, *12*, 3875–3885.

[16] J. A. Carrasco, R. Sanchis-Gual, A. S.-D. Silva, G. Abellán, E. Coronado, *Chem. Mater.* **2019**, *31*, 6798–6807.

[17] S. Sun, C. Lv, W. Hong, X. Zhou, F. Wu, G. Chen, *ACS Appl. Energy Mater.* **2019**, *2*, 312–319.

[18] Y. Dong, S. Komarneni, F. Zhang, N. Wang, M. Terrones, W. Hu, W. Huang, *Applied Catalysis B: Environmental* **2020**, *263*, 118343.

[19] X. P. Wang, H. J. Wu, S. B. Xi, W. S. V. Lee, J. Zhang, Z. H. Wu, J. O. Wang, T. D. Hu, L. M. Liu, Y. Han, S. W. Chee, S. C. Ning, U. Mirsaidov, Z. B. Wang, Y. W. Zhang, A. Borgna, J. Wang, Y. H. Du, Z. G. Yu, S. J. Pennycook, J. M. Xue, *Energy & Environmental Science* **2020**, *13*, 229–237.

[20] X. Wang, S. Xi, W. S. V. Lee, P. Huang, P. Cui, L. Zhao, W. Hao, X. Zhao, Z. Wang, H. Wu, H. Wang, C. Diao, A. Borgna, Y. Du, Z. G. Yu, S. Pennycook, J. Xue, *Nat Commun* **2020**, *11*, 4647.

[21] R. Ma, Z. Liu, K. Takada, K. Fukuda, Y. Ebina, Y. Bando, T. Sasaki, *Inorg. Chem.* **2006**, *45*, 3964–3969.

[22] Y. Du, D. O'Hare, *Inorg. Chem.* **2008**, *47*, 3234–3242.

[23] D. Hunt, V. Oestreicher, M. Mizrahi, F. G. Requejo, M. Jobbágy, *Chemistry – A European Journal* **2020**, *26*, 17081–17090.

[24] V. Oestreicher, G. Abellán, E. Coronado, *physica status solidi (RRL) – Rapid Research Letters* **2020**, *14*, 2000380.

[25] R. Sanchis-Gual, D. Hunt, C. Jaramillo, Á. S.-D. Silva, M. Mizrahi, C. Marini, V. Oestreicher, G. Abellán, **2022**, DOI 10.26434/chemrxiv-2022-rcq28.

[26] G. J. de A. A. Soler-Illia, M. Jobbágy, A. E. Regazzoni, M. A. Blesa, *Chem. Mater.* **1999**, *11*, 3140–3146.

[27] J. Liang, R. Ma, N. Iyi, Y. Ebina, K. Takada, T. Sasaki, *Chem. Mater.* **2010**, *22*, 371–378.

[28] D. S. Hall, D. J. Lockwood, C. Bock, B. R. MacDougall, *Proceedings of the Royal Society A: Mathematical, Physical and Engineering Sciences* **2015**, *471*, 20140792.

[29] Q. Wang, D. O'Hare, *Chem. Rev.* **2012**, *112*, 4124–4155.

[30] M. Taibi, S. Ammar, N. Jouini, F. Fiévet, P. Molinié, M. Drillon, *J. Mater. Chem.* **2002**, *12*, 3238–3244.

[31] M. Taibi, N. Jouini, P. Rabu, S. Ammar, F. Fiévet, *J. Mater. Chem. C* **2014**, *2*, 4449–4460.

[32] P. V. Kamath, G. H. Annal Therese, J. Gopalakrishnan, *Journal of Solid State Chemistry* **1997**, *128*, 38–41.

[33] R. D. Shannon, *Acta Crystallographica Section A* **1976**, *32*, 751–767.

[34] V. Oestreicher, I. Fábregas, M. Jobbágy, *J. Phys. Chem. C* **2014**, *118*, 30274–30281.

[35] N. Arencibia, V. Oestreicher, F. A. Viva, M. Jobbágy, *RSC Advances* **2017**, *7*, 5595–5600.

[36] Z. Liu, R. Ma, M. Osada, K. Takada, T. Sasaki, *J. Am. Chem. Soc.* **2005**, *127*, 13869–13874.

[37] Z. Liu, R. Ma, M. Osada, N. Iyi, Y. Ebina, K. Takada, T. Sasaki, *J. Am. Chem. Soc.* **2006**, *128*, 4872–4880.

[38] M. C. Biesinger, B. P. Payne, A. P. Grosvenor, L. W. M. Lau, A. R. Gerson, R. St. C. Smart, *Applied Surface Science* **2011**, *257*, 2717–2730.

[39] V. Oestreicher, C. Dolle, D. Hunt, M. Fickert, G. Abellán, *Nano Materials Science* **2022**, *4*, 36–43.

[40] J. R. Neilson, B. Schwenzer, R. Seshadri, D. E. Morse, *Inorg. Chem.* **2009**, *48*, 11017–11023.

[41] V. Oestreicher, D. Hunt, R. Torres-Cavanillas, G. Abellán, D. A. Scherlis, M. Jobbágy, *Inorg. Chem.* **2019**, *58*, 9414–9424.

[42] V. Oestreicher, D. Hunt, C. Dolle, P. Borovik, M. Jobbágy, G. Abellán, E. Coronado, *Chemistry – A European Journal* **2021**, *27*, 921–927.

[43] Q. He, Y. Wan, H. Jiang, Z. Pan, C. Wu, M. Wang, X. Wu, B. Ye, P. M. Ajayan, L. Song, *ACS Energy Lett.* **2018**, *3*, 1373–1380.

[44] R. W. Cairns, E. Ott, *J. Am. Chem. Soc.* **1933**, *55*, 527–533.

[45]   J. Zemann, *Acta Crystallographica* **1965**, *18*, 139–139.
[46]   T. N. Ramesh, P. V. Kamath, C. Shivakumara, *Acta Cryst B* **2006**, *62*, 530–536.
[47]   Y. Wang, M. Qiao, Y. Li, S. Wang, *Small* **2018**, *14*, 1800136.
[48]   A. S.-D. Silva, V. Oestreicher, E. Coronado, G. Abellán, *Dalton Transactions* **2022**, *51*, 4675–4684.
[49]   Z. Lu, W. Xu, W. Zhu, Q. Yang, X. Lei, J. Liu, Y. Li, X. Sun, X. Duan, *Chem. Commun.* **2014**, *50*, 6479–6482.
[50]   J. Zhang, J. Liu, L. Xi, Y. Yu, N. Chen, S. Sun, W. Wang, K. M. Lange, B. Zhang, *J. Am. Chem. Soc.* **2018**, *140*, 3876–3879.
[51]   M. Steimecke, G. Seiffarth, C. Schneemann, F. Oehler, S. Förster, M. Bron, *ACS Catal.* **2020**, *10*, 3595–3603.
[52]   H. Radinger, P. Connor, S. Tengeler, R. W. Stark, W. Jaegermann, B. Kaiser, *Chem. Mater.* **2021**, *33*, 8259–8266.
[53]   S. Klaus, Y. Cai, M. W. Louie, L. Trotochaud, A. T. Bell, *J. Phys. Chem. C* **2015**, *119*, 7243–7254.
[54]   R. Ma, Z. Liu, K. Takada, N. Iyi, Y. Bando, T. Sasaki, *J. Am. Chem. Soc.* **2007**, *129*, 5257–5263.
[55]   R. Ma, K. Takada, K. Fukuda, N. Iyi, Y. Bando, T. Sasaki, *Angewandte Chemie International Edition* **2008**, *47*, 86–89.
[56]   Y. He, X. Liu, G. Chen, J. Pan, A. Yan, A. Li, X. Lu, D. Tang, N. Zhang, T. Qiu, R. Ma, T. Sasaki, *Chem. Mater.* **2020**, *32*, 4232–4240.
[57]   T. W. Capehart, J. F. Herbst, R. K. Mishra, F. E. Pinkerton, *Phys. Rev. B* **1995**, *52*, 7907–7914.
[58]   R. Barnard, C. F. Randell, F. L. Tye, *J Appl Electrochem* **1980**, *10*, 109–125.
[59]   J. McBreen, W. E. O'Grady, G. Tourillon, E. Dartyge, A. Fontaine, K. I. Pandya, *J. Phys. Chem.* **1989**, *93*, 6308–6311.
[60]   Y.-F. Li, J.-L. Li, Z.-P. Liu, *J. Phys. Chem. C* **2021**, *125*, 27033–27045.
[61]   N. Tarutani, Y. Tokudome, M. Jobbágy, G. J. A. A. Soler-Illia, M. Takahashi, *Journal of Materials Chemistry A* **2019**, *7*, 25290–25296.